# Wettability and corrosion resistance of zirconium nitride films obtained via reactive high-power impulse magnetron sputtering

Special Collection: Functional Coatings

José D. Castro ✉ 🔘 ; Beatriz Pinto; Fábio Ferreira 🔘 ; R. Serra 🔘 ; S. Carvalho 🔘

Check for updates

View Online    Export Citation

## Articles You May Be Interested In

Effect of bias voltage and nitrogen content on the morphological, structural, mechanical, and corrosion resistance properties of micro-alloyed $Ti_{1-x}Al_{0.8x}P_{0.2x}N_y$ films deposited by high power impulse magnetron sputtering

*J. Vac. Sci. Technol. A* (December 2022)

Tailoring structure, morphology, and tribo-mechanical properties of HiPIMS-deposited $Cr_xN_y$ coatings for enhanced performance in wear and corrosion protection

*J. Vac. Sci. Technol. A* (May 2024)

# Wettability and corrosion resistance of zirconium nitride films obtained via reactive high-power impulse magnetron sputtering

View Online    Export Citation    CrossMark

José D. Castro,[1,a] [iD] Beatriz Pinto,[1] Fábio Ferreira,[1,2,3] [iD] R. Serra,[1] [iD] and S. Carvalho[1] [iD]

## AFFILIATIONS

[1]CEMMPRE Mechanical Engineering Department, University of Coimbra, 3030-788 Coimbra, Portugal
[2]LED&Mat-IPN, Instituto Pedro Nunes, Laboratório de Ensaios Desgaste e Materiais, Rua Pedro Nunes, 3030-199 Coimbra, Portugal
[3]Walker Department of Mechanical Engineering, The University of Texas at Austin, Austin, Texas 78712

**Note:** This paper is a part of the 2023 Special Topic Collection on Functional Coatings.
[a]**Author to whom correspondence should be addressed:** uc2021120076@student.uc.pt

## ABSTRACT

One of the main problems in ships is corrosion, which reduces the lifetime usage of ship parts and increases maintenance costs. Ceramic coatings can contribute to solving this situation. Zirconium nitrides obtained by reactive unbalanced magnetron sputtering technology are largely reported as coatings with high corrosion resistance. The present study used high-power impulse magnetron sputtering in a reactive atmosphere (R-HiPIMS), varying the nitrogen amount. SEM, EDS, XRD, AFM, and contact angle measurements were used to assess the obtained coatings' performance. Corrosion resistance was evaluated using electrochemical impedance spectroscopy (EIS) (up to 168 h exposure) and potentiodynamic polarization (PP) in NaCl (3.5% wt.—"artificial seawater") solution. According to the results, cross section micrographs showed strong densification of ZrN films regardless of the nitrogen amount. Besides, nitrogen increases during deposition influenced the drop of applied peak power ($P_p$) to the target and, consequently, influenced other film properties, such as roughness, wettability, and corrosion resistance. PP and EIS tests demonstrate the protective behavior of films under artificial seawater exposure. The results prove that the implementation of HiPIMS technology to obtain ZrN films could contribute to increasing the corrosion resistance of coated ship metallic parts and, hence, help maritime transportation to reduce maintenance time and cost.

## I. INTRODUCTION

The marine ecosystem has been demonstrated to be very aggressive for ship metallic parts, provoking a ship's immobilization for maintenance tasks and, consequently, an increase of cost in the operation and transportation of merchandise. Among the metallic components in ships, sea chest gratings are prone to two main problems: corrosion and biofouling. Biofouling is the accumulation of aquatic organisms over surfaces exposed to oceans or any other water body.[1] Besides biofouling accumulation, the marine environment provokes corrosion itself, and this phenomenon cost is close to 2.5 trillion USD in 2016 according to the report of the National Association of Corrosion Engineers.[2] Developing surfaces to overcome these problems is undoubtedly a big priority for the naval industry.

Currently, coatings are the main prospective systems used by the maritime industry to avoid corrosion. However, some of the currently used paints are composed of toxic products that interfere with the marine environment's stability and biodiversity. Isolation effect from the environment, hydrophobicity, low roughness, and other features made paints the perfect candidate for ships. However, its heavy pollution of the seas and harmful effects on sealife provoked more substantial control by the International Maritime Organization. It is well known that paints have poor mechanical and antidegradation properties;[3] thus, they do not offer that much long-lasting protection against corrosive agents.

In this line, other processes and products have been tried to take the place of paints in the naval industry, such as nano-

texturization,[4] bio-inspired surfaces,[5,6] or biocide-release coatings.[7] Among the possible solutions to get a multifunctional surface against biofouling and corrosion, films obtained by physical vapor deposition (PVD) seem to have the potential to replace paints. By its nature, PVD films offer processing advantages compared to other technologies mentioned before, such as fine control over chemical composition, thickness, microstructure, and architecture.[1,8–11]

Some authors' research works studied surfaces with some multifunctionality by PVD, especially transition metal oxide/nitride-based coatings obtained by Direct Current Magnetron Sputtering (dcMS) technology. It is well known that these materials are largely used in the industry for their hardness,[12] wear resistance,[13,14] and high corrosion resistance.[15,16] Lately, high power impulse magnetron sputtering (HiPIMS) was employed to improve the overall performance of the obtained films[17] but as a drawback, it presents lower deposition rates than dcMS. Its potential applications have been explored by several authors such as Castilho et al.,[18] who obtained $CrN/Cr_{1-x}Al_xN$ superlattices through a hybrid magnetron sputtering process (HiPIMS/dcMS), capable of yielding more competitive deposition rates than only pure HiPIMS films. The obtained films showed potential use for emissions reduction in combustion engines by improving the piston rings performance in tribological, anticorrosion, and resistance to plastic deformation compared to the tested commercial solution (CrN obtained by cathodic arc deposition). Abegunde et al.[19] compared TiAl(P)N films obtained by dcMS and HiPIMS. Their results pointed out a systematic improvement in mechanical properties and corrosion resistance in the coatings obtained by HiPIMS, compared with dcMS. Alves et al.[20] deposited Ta and $Ta_{1-x}O_x$ coatings by HiPIMS in deep oscillation magnetron sputtering (DOMS) mode. According to their results, the addition of oxygen promoted more dense morphologies and higher corrosion resistance. Also, Sousa et al.[21] obtained TiAlSiN coatings over duplex stainless steel alloy LDX 2101 by dcMS and HiPIMS to evaluate the wear behavior and cutting performance. The coatings obtained through HiPIMS exhibited low wear rates and improved mechanical performance, highlighting the advantage of using HiPIMS for coated cutting tools. As described, HiPIMS technology has the potential to obtain multifunctionality coatings, with enhanced properties compared with dcMS.

The present study intends to explain the impact of nitrogen content on ZrN film properties, especially in wettability and anticorrosive (against saline solution), using HiPIMS technology in the DOMS mode. For comparison purposes, a ZrN film was obtained by dcMS, employing the same average power and working pressure used for the DOMS films. This new paradigm could open new possibilities to understand the mechanism of improvement (or detriment) of ZrN film features when nitrogen increases using DOMS technology.

## II. EXPERIMENT

### A. Deposition parameters

The films were deposited in a high vacuum chamber through HiPIMS (Cyprium™ III plasma generator, Zpulser Inc.) technology in the DOMS mode using a reactive atmosphere (i.e., R-HiPIMS).

A single Zr target (99.9% purity) with a $150 \times 150$ mm$^2$ area was used. Typical signal waves of oscillating discharge voltage and current of DOMS processing are shown in Fig. 1. These pulses are composed of a big package of 27 sequential individual oscillations [Fig. 1(a)]. The current and the voltage increase progressively during the on-time ($t_{ON}$) up to reach the maximum values ($I_p$ and $V_p$, respectively). The peak power ($P_p$) was calculated in every deposition as the product of $V_p$ and $I_p$. Later, these values decrease successively until they go back to zero during the off-time ($t_{OFF}$). As with any duty cycle, the sum of these two times will be the pulse period ($T = t_{ON} + t_{OFF}$). During the depositions, $t_{ON}$ (12 $\mu$s) and T (36 $\mu$s), as well as the pulse duration (D = 1000 $\mu$s) were
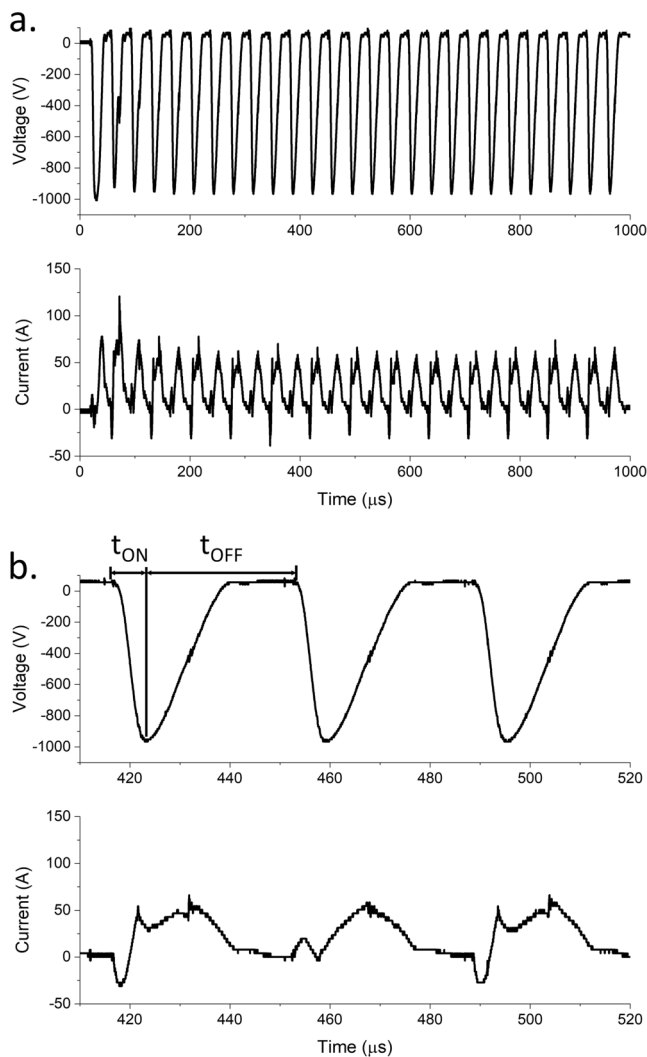


**FIG. 1.** Typical target current and voltage oscillation waveforms of a DOMS pulse (D = 1000 $\mu$s) obtained during the films' depositions (a) and magnification of three consecutive pulses in the 100 $\mu$s range (b) (P = 0.4 Pa; frequency— $F_i$ = 132 Hz; $t_{ON}$ = 12 $\mu$s; T = 36 $\mu$s).

06 November 2024 11:23:08

**TABLE I.** Sputtering partial pressures and current and voltage wave details for depositions of the present study.

| Pressure (Pa) | Sample | $P_{Ar}$[a] (Pa) | $P_{N2}$[a] (Pa) | N₂/Ar ratio | $F_i$ (Hz) | $V_p$[b] (V) | $I_p$[b] (A) | $P_p$ (kW) |
|---|---|---|---|---|---|---|---|---|
| 0.4 | DOMS-ZrN-30 | 0.33 | 0.07 | 0.2 | 131 | −1066 | 126 | 134 |
|  | DOMS-ZrN-40 | 0.29 | 0.11 | 0.4 | 132 | −1063 | 109 | 116 |
|  | DOMS-ZrN-80 | 0.17 | 0.23 | 1.4 | 138 | −1054 | 93 | 98 |

[a]Measured from the respective gas flow.
[b]Extracted from a ZPulser generator power source controller.

constant. The power supply had an internal d.c. power supply, which was set up at 300 V (DC$_{int}$) in all depositions. All the films were made using a 1200 W average power ($P_a$), and the working pressure was kept at 0.4 Pa. This pressure was adjusted as nitrogen was introduced into the deposition chamber, reducing the argon flow to compensate. No bias voltage was used in HiPIMS depositions. For comparison, a ZrN film (labeled as dcMS-ZrN) by reactive direct current magnetron sputtering (dcMS) was deposited using 1200 W power and employing a −50 V bias voltage according to the optimized conditions in our previous published works.[22,23] The used partial pressures were 0.33 Pa for argon and 0.07 for nitrogen (measured from the respective gas flows). All depositions were carried out without external heating. Additional parameters are shown in Table I.

Silicon wafers ⟨100⟩ and stainless steel (316L) specimens ($20 \times 20 \times 2\,mm^3$) were chosen to be coated. Substrates were washed in distilled water, acetone, and ethanol ultrasonically for 10 min each. Stainless steel grade 316L (SS316L) was selected to simulate the material used in sea chest gratings. The substrates were held in rotating support at 23.5 rpm and localized in the center of the chamber at an 80 mm distance from the target. The substrate holder possesses four faces with a $30 \times 110\,mm^2$ area in each one and, hence, can support 20 specimens in each deposition. In the first stage, the chamber always attained base pressures below $10^{-4}$ Pa, being the reactive atmosphere composed of a N₂ + Ar mixture, controlled individually. To improve the adhesion of the nitride films, a pure Zr layer was deposited (~300 nm thickness) keeping the same parameters in the used power source ($P_a$, T, etc.).

Before each deposition, substrates were cleaned by an etching process in an argon atmosphere (0.3 Pa) for 60 min with a d.c. pulsed power source connected to the substrate holder using −350 V with 1616 ns and 120 kHz as pulse reverse time and frequency, respectively.

### B. Coatings characterization

Morphology and cross section profiles were studied by scanning electron microscopy (SEM), and the chemical composition was assessed by energy-dispersive spectroscopy (EDS) at 15 kV. The film structure was analyzed by glancing incidence x-ray diffraction in the PANalytical X-pert PRO MPD equipment, which was set up in Θ = 3°. CuKα (λ = 1.5406 nm) radiation was operated at 45 kV and 40 mA with 0.02° step size in coated Si substrates. To fit the spectra, the Pseudo-Voigt function was used to calculate the crystallite size using the Scherrer formula in the preferential growth peaks. The residual stresses were established by employing the methodology suggested by Shiri et al.[24] and by applying Stoney's equation.[25]

The surface roughness of the films was assessed by atomic force microscopy (Bruker Innova) at room temperature with a Si cantilever with less than 8 nm tip radius, operated in a tapping mode. Three measurements were performed to evaluate the average surface roughness ($S_a$) in all samples according to the ISO 25178 standard and holding a $3 \times 3\,\mu m^2$ area. All obtained images were post-processed using GWYDDION software.

The wettability measurements were acquired by optical contact angle measurements (Dataphysics OCA20 equipment). For calculations, ultrapure water (99,99%), glycerol, and α-bromonaphthalene were used to obtain surface-free energies according to the Owens–Wendt–Rabel–Kaeble (OWRK) method.[26–28] Besides, artificial seawater (or brine—3.5% w/w NaCl solution) was used to assess film interaction to a simulated work condition. The surface tension of used liquids was extracted from reference values in other studies.[8,29] The drop volume was kept below 10 μl to prevent any possible interferences in the contact angle measurements by the drop weight.

Corrosion behavior was carried out by two different tests: potentiodynamic polarization (PP) and electrochemical impedance spectroscopy (EIS). In all these tests, a NaCl (3.5 wt. %) solution was used to simulate the exposure of the film to the seawater for the period of 168 h in a static state (EIS measurements), naturally ventilated, and always assuring the electrical contact electrolyte/samples. All measurements were performed in a potentiostat (Gamry 600) connected to an electrochemical cell at room temperature (20 °C). A three-electrode configuration was used with the studied sample as the working electrode (exposed area = $0.28\,cm^2$), a platinum sheet as the counter electrode, and a saturated calomel electrode (SCE) as the reference electrode. The potentials were measured against and referred to the standard potential of the SCE and labeled as $E_{ref}$ in the obtained results (0.245 V vs the standard hydrogen electrode). The PP measurements were performed between −500 and 500 mV vs $E_{ref}$ with a 1 mV/s scan rate. EIS was performed by acquiring 10 points by decade and applying 10 mV rms, between 100 kHz and 0.01 Hz. In all corrosion tests, the samples were always exposed at 3600 s to establish a steady state open circuit potential (OCP) before every measurement (<0.01 mV/s variation). At least three electrochemical tests were performed for each coating condition. The ASTM G102-89 standard was applied to fit the data from Tafel slopes and to calculate the corrosion rates.[30]

**TABLE II.** Chemical composition, thickness, and deposition rates of the coatings.

| Sample | Zr (at. %) | N (at. %) | O (at. %) | Zr/(N + O) ratio | Thickness (nm) | Dep. rate ($\mu$m/h) |
|---|---|---|---|---|---|---|
| dcMS-ZrN | 49 ± 2 | 47 ± 2 | 4 ± 0 | 0.96 | 798 ± 7 | 1.1 |
| DOMS-ZrN-30 | 47 ± 3 | 51 ± 2 | 2 ± 0 | 0.88 | 1033 ± 5 | 0.8 |
| DOMS-ZrN-40 | 47 ± 3 | 50 ± 2 | 3 ± 0 | 0.88 | 1039 ± 6 | 0.7 |
| DOMS-ZrN-80 | 43 ± 3 | 54 ± 3 | 3 ± 0 | 0.75 | 883 ± 5 | 0.3 |

## III. RESULTS AND DISCUSSION

### A. Chemical and surface characterization

The thickness, deposition rate, and chemical composition of the obtained films are presented in Table II. The deposition rate by DOMS decreased in comparison with the dcMS film. When the $N_2$/Ar ratio was constant (0.2 for DOMS-ZrN-30 and dcMS-ZrN), the deposition rate decreased by ~27% in the DOMS film (see Table II). Oliveira *et al.*[31] reported that the deposition rate in TiN films decreased when they were deposited by DOMS around 50% in comparison with their counterpart deposited by dcMS at the same nitrogen fraction ($f_{N_2}$ = $N_2$ flow/Ar + $N_2$ flows). The authors ascribed this decrease to several effects during the HiPIMS process such as the yield effect (linked to higher deposition voltages) and the return effect (related to metallic ionized species which return to the target), which could be present during the film processing of this study. On the other hand, as the $N_2$/Ar ratio increases in the DOMS films, the deposition rate decreases consistently. The target is poisoned by nitrogen, but this effect will be discussed next.

All the zirconium nitride films deposited by HiPIMS are close to the stoichiometric composition except for the sample deposited with the highest nitrogen flow that becomes over-stoichiometric, being well correlated with a significant decrease in the deposition rate (see Table II). The higher grade of over-stoichiometric composition in the DOMS films could be associated with the bombardment of the film by the $N^+$ ions, present in the HiPIMS ionized plasma.[31] In HiPIMS, current discharges are influenced by the self-sputtering and gas recycling processes.[32] The first one occurs when the target ions impinge over the target itself and the second one occurs when the gas present in the process is ionized and re-used to sputter material. Table I shows the reduction of current (i.e., $I_p$) as the nitrogen flow increased in the deposition. This is provoked by the introduction of new particles into the deposition (i.e., nitrogen) and respective influence roles in the discharge. Target poisoning increases gas recycling but reduces the self-sputtering phenomenon, reducing the deposition rate and the incorporation of Zr on the films. With the target poisoned, the formation of compounds (nitrides) on the target surface is quite possible because an ionized plasma is present. According to Anders,[32] the HiPIMS process in a reactive atmosphere shows a decrease in sputtering yields (i.e., in sputtering rates) due to the bond strength of compounds which is higher, if this is compared to the bond strength of metals. That means the energy needed to sputter material toward the substrate must be higher which traduces in a reduction of the sputtering efficiency.

The coatings' surface morphology and cross section microstructure are shown in Fig. 2. The dcMS film [Fig. 2(a)] exhibits a typical columnar growth profile, exhibiting columns extending along the film thickness and corresponding to zone 1 of the Thornton diagram.[33] On the other hand, the HiPIMS films show different growth profiles also dependent on the nitrogen amount in the deposition. DOMS-ZrN-30 [Fig. 2(c)] displays dense packed fibrous grains that shift to a dense and featureless growth profile for the highest nitrogen flow [DOMS-ZrN-80 sample in Fig. 2(g)]. According to Anders diagram,[34] the DOMS films are localized in zone T, which is localized in an intermediate range of normalized energy flux (E*) and, hence, is related to the heating and displacement caused by the kinetic energy of the bombarding particles and generalized temperature (T*), correlated with the temperature of the particles plus the temperature shift provoked by the potential energy of particles arriving the surface.[34] Regarding the top views, the dcMS film [Fig. 2(b)] shows voided boundaries as zone 1 in the Thornton diagram describes.[33] On the other hand, the DOMS films shift from like cauliflower surfaces [Fig. 2(d)] to a finest grainy appearance as nitrogen increases [Fig. 2(h)], in agreement with zone T of Anders diagram.[34]

### B. Structural characterization

Figure 3 displays x-ray diffractograms of the films. The diffractograms exhibit the evolution of the crystallographic structure of the coatings, which are coherent mainly with two patterns: Rock-salt type fcc-ZrN (ICDD card no. 035-0753) and orthorhombic-$Zr_3N_4$ (ICDD card no. 087-0843). The effect of nitrogen increase in sputtered $ZrN_x$ coatings structure was studied by Lamni *et al.*[35] and their results pointed out that when the film is over stoichiometric (x > 1.0), $Zr_3N_4$ phase (labeled as * in Fig. 3) presence affects the film structure and, consequently, provokes the fcc-ZrN plane peaks to broaden. Besides, low amounts of oxygen in ZrN films also provoke the appearance of the $Zr_3N_4$ phase as discussed by several authors,[22,36] as also stated in the dcMS deposited film. At 63.33°, the detected peak coincides with several $Zr_3N_4$ reflections. Table II demonstrates that the atomic percentage of non-metallic elements was always higher than Zr [Zr/(N + O) ratio < 1] which can influence the film structures by these elements. Besides, the evident broadening of peaks in the dcMS and DOMS films could result in a mixed mechanism in the mentioned phenomena. According to some authors, the $Zr_3N_4$ phase is formed by the occupancy of N atoms in interstitial positions, and it is considered a nitride structure doped poorly by oxygen.[22,35,36]

On the other hand, the films showed typical ZrN peaks presented at 33.89°, 39.32° (exclusively in the dcMS film), and 56.45° corresponding to the (111), (200), and (220) planes, respectively. Figure 3 shows that the dcMS and DOMS films with low nitrogen
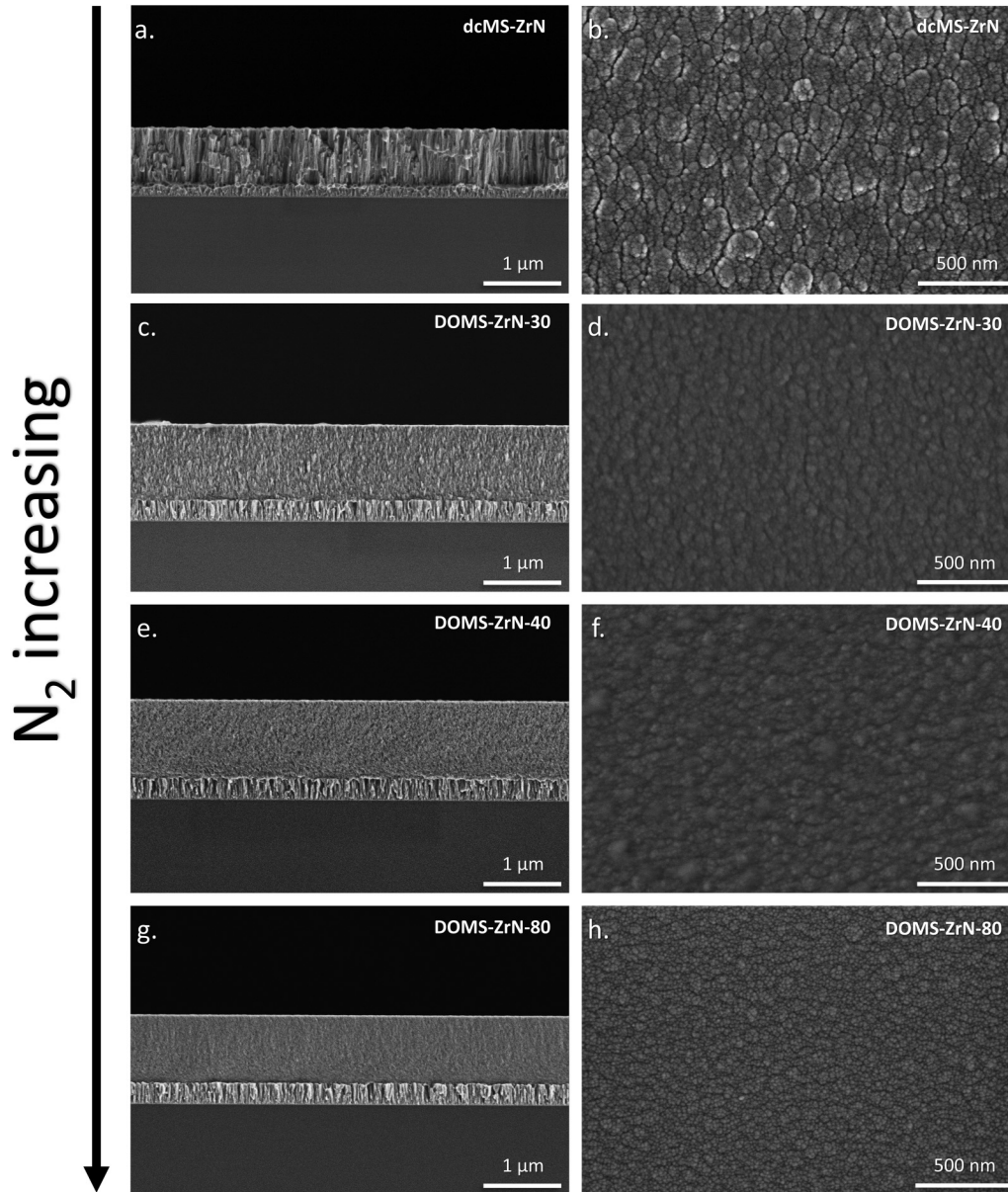
06 November 2024 11:23:08

**FIG. 2.** Cross section (left) and top view (right) SEM images of the films obtained at 0.4 Pa working pressure: dcMS-ZrN [(a) and (b)], DOMS-ZrN-30 [(c) and (d)], DOMS-ZrN-40 [(e) and (f)], and DOMS-ZrN-80 [(g) and (h)].

content exhibited the (111) plane as the preferential one, as described by several authors.[37] Only DOMS-ZrN-80 exhibited a different preferential orientation, the (220) plane. The crystallite size reduction in the (111) plane evidences this phenomenon. This varied from 7 nm at dcMS-ZrN to 4 nm at DOMS-ZrN-40. Besides, the DOMS-ZrN-80 film showed a 38 nm crystallite size when the preferential orientation changed to the (220) plane. These changes in texture are related to the difference in the ion/atom ratio during

deposition. As more nitrogen was introduced, less available zirconium was inside the deposition chamber and the texture was modified as a consequence.[38] Moreover, the preferred orientation in sputtered metallic nitrides depends on the surface energy and the strain energy.[39,40] At small surface energies, the (100) plane is expected in a NaCl-type structure and implies a low residual stress condition. On the contrary, the (111) plane is possible at higher surface energies.[40] Also, the orientation change in ZrN films is
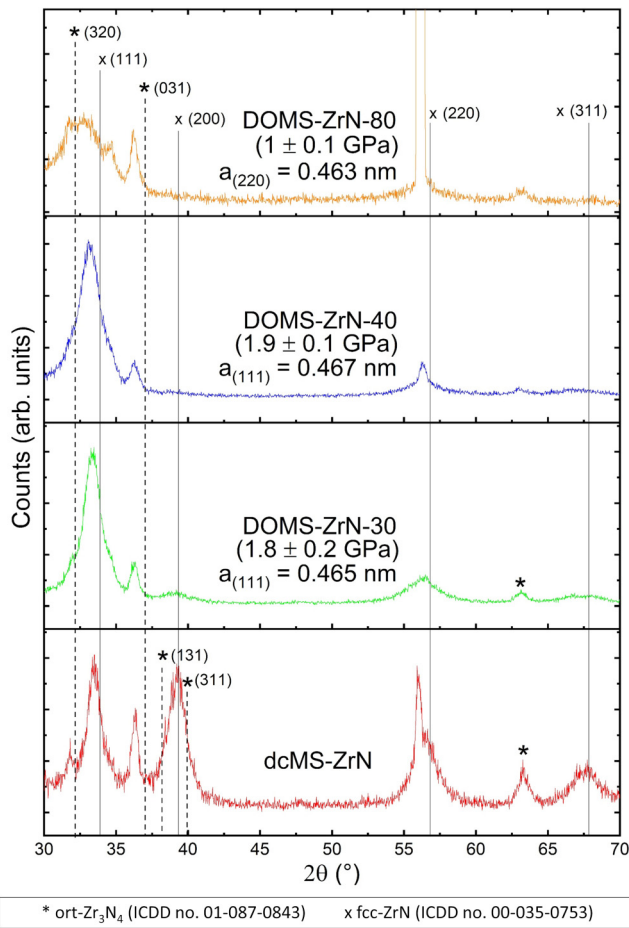
**41**, 023106-5

**FIG. 3.** XRD diffractograms of the films. Values between parentheses represent the measured compressive residual stress in the method proposed by Shiri *et al.* (Ref. 24) and the "a" values represent the lattice parameter calculated from the preferential growth peak.



**FIG. 4.** Surface free energy, average surface roughness (a), and contact angle measurements (b) of the coatings. The dashed line in (a) designates the limit between hydrophobic (>90°) and hydrophilic conditions.

related to the carried energy toward the film. Hence, the plane with the lowest surface energy, the (200) plane, becomes the preferential growth plane.[41] It is possible to suggest that the shift in the preferential plane showed by DOMS-ZrN-80 is related to the decrease of $P_P$ and, hence, the delivered energy to the film may be enough to provoke the growth of the (220) plane, which has a lower surface energy than the (111) plane.

Systematically, the peaks of all films exhibited a deviation for minor 2θ positions, which is explained by the existence of compressive stresses, commonly reported in sputtered coatings. The distortion of the ZrN lattice parameter changed in the range between 4.63 and 4.67 Å (lattice parameter of ZrN pattern, a = 4.58 Å free of stresses) as shown in other coatings obtained by HiPIMS using DOMS.[42] Lattice deformation is directly influenced by compressive residual stress as exposed in Fig. 3, which is provoked by the mentioned phenomenon (interstitial atoms in the ZrN lattice).
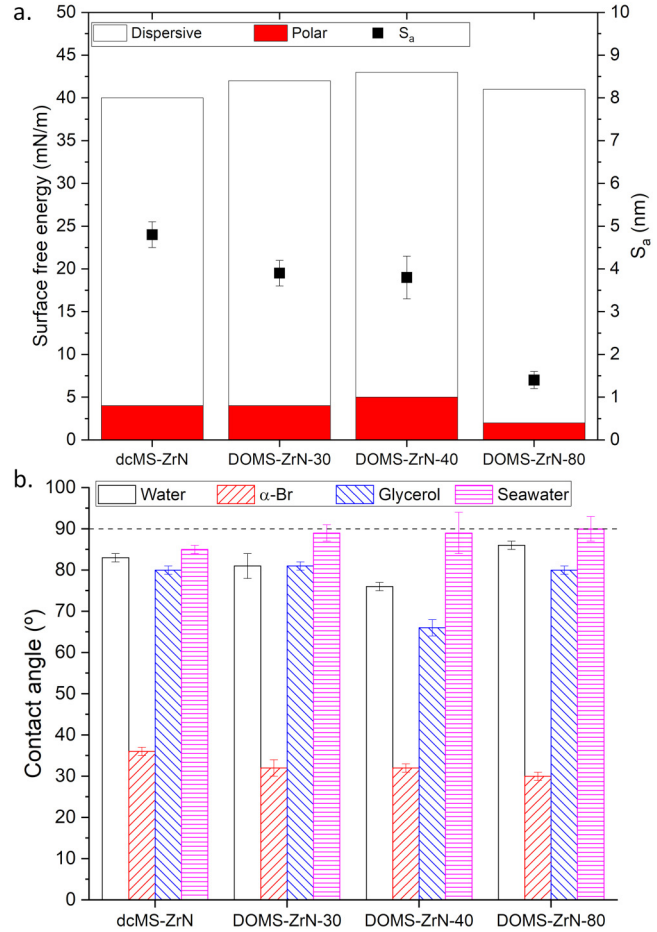
## C. Roughness, surface energy, and wettability

Surface roughness, liquid contact angles, and surface free energy (SFE) obtained by the ORWK model are displayed in Fig. 4. All the samples exhibit low roughness values (<10 nm) and are mostly "liquidphilic" (contact angles < 90°). DOMS-ZrN-30 and DOMS-ZrN-40 exhibit $S_a$ values close to each other (~5 nm); on the other hand, DOMS-ZrN-80 exhibits the lowest roughness value (<2 nm). Concerning the dcMS film, the roughness values are slightly higher than DOMS-ZrN-30 and DOMS-ZrN-40 [see Fig. 4(a)].

Regarding the contact angles taken with artificial seawater, the DOMS films exhibited values close to the limit between philic/phobic behavior (around 90°). On the other hand, the dcMS film shows a hydrophilic nature, similar to the Wenzel model.[43] The film compactness (at least in DOMS films) and the differences in roughness influence this behavior. Meanwhile, the SFE did not show significant differences either in their components (polar and

06 November 2024 11:23:08

dispersive) or their total values (see Fig. 4) regardless of the film processing (dcMS or DOMS) as well as nitrogen content, which suggests the non-importance of the chemical component of wettability in these coatings.

To assess the artificial seawater/surface interaction through the work of adhesion ($W_a$), the postulation of Jin et al.[44] was used, which is based on Young equations and used extensively in the literature.[8,45] This model considers solid and liquid's polar and dispersive components, interacting solely between them. Even though the liquid has surface tension (ST) and the solid has SFE, this is an intrinsic issue in the ORWK model.[46] Following the postulation of Jin et al.,[44] it is possible to use the maximum thermodynamic work of adhesion ($W_a$) based on Dupree's equation,[47] according to the following expression:

$$W_a = \gamma_s + \gamma_l - \gamma_{sl}. \tag{1}$$

This equation is adapted for a solid/liquid interface and $\gamma_s$ is the SFE of the solid, $\gamma_l$ is the ST of the liquid, and $\gamma_{sl}$ is the interfacial free energy. The last one varies with the liquid in contact with the surface (as well as its contact angle).

Table III exhibits the calculated parameters using the ORWK model from the measured contact angles [for $\gamma_s$—values from Fig. 4(a)], the Young equation (for $\gamma_{sl}$), and Eq. (1). The artificial seawater surface tension ($\gamma_l = 73.2$ mN/m) used for this calculation was recently published in our past work.[8] According to Table III, the dcMS films show a higher $W_a$ than the DOMS films, achieving up to ∼8.5% of $W_a$ reduction and demonstrating a systematic "seawater rejection" from the DOMS films. DOMS-ZrN-80 displayed the lowest $W_a$ (73 mN/m) in agreement with its highest seawater CA (90°).

## D. Corrosion tests

PP tests were done to analyze the corrosion mechanisms and potentials of the films when they are exposed to artificial seawater. Obtained results after these tests are exhibited in Fig. 5 and Table IV.

The SS316L substrate exhibited the worst corrosion behavior in comparison to the coated samples and it is the only one which showed some pitting events at high potentials (between 400 and 500 mV). Assessing the films, DOMS-ZrN-80 exhibits the noblest behavior, which shows the cathodic/anodic shift at −212 mV. On contrary, dcMS-ZrN displays the most active behavior (shift at −255 mV). Concerning the corrosion current densities ($J_{corr}$), DOMS films have shown a significant decrease compared to the

dcMS films and the uncoated substrate. This behavior is reflected in the improvement of corrosion resistance. This is demonstrated by a reduction in the corrosion rate (calculated using the ASTM G102-89 standard procedure[30]) by almost ∼2.6 times in the DOMS films when compared to its counterpart obtained by dcMS, and close to ∼3.3 times when it is compared to the uncoated substrate (see Table IV—average corrosion rate value of DOMS films). Another remarkable fact was that none of the films did surpass the passivation region, which would be a strong indicator of film damage or re-activation of anodic processes.

Though SS316L is known as an anticorrosion material that forms an outermost chromium oxide ($Cr_2O_3$) layer, as the self-protection mechanism[48] is mechanically poor, and any external factor (like suspended particles) creating some erosion or wear could affect its performance and, hence, compromise the substrate protection. Besides the lower corrosion rates, the films possess a thicker ceramic layer, which proves to be an effective protection layer for SS316L against artificial seawater. This ceramic nature is
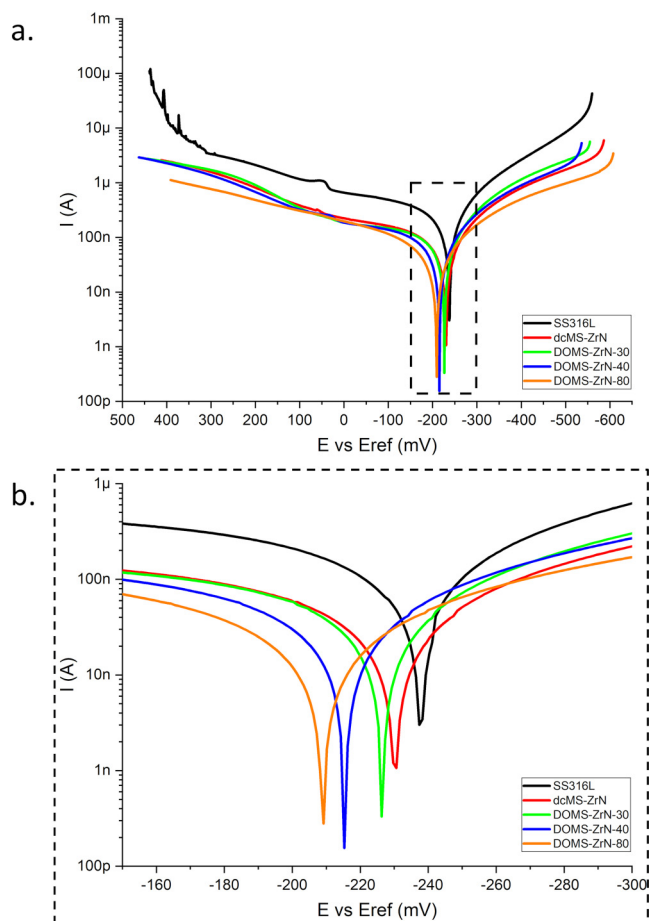
**FIG. 5.** PP curves of the films immersed in 3.5% w/w NaCl solution (a) and magnification of the anodic/cathodic change region (b).

**TABLE III.** Artificial seawater contact angle (SCA), surface free energy ($\gamma_s$), interfacial free energy ($\gamma_{sl}$), and work of adhesion ($W_a$) of the films.

| Sample | SCA (deg) | $\gamma_s$ (mN/m) | $\gamma_{sl}$ (mN/m) | $W_a$ (mN/m) |
|---|---|---|---|---|
| dcMS-ZrN | 85 ± 1 | 40 | 34 | 80 |
| DOMS-ZrN-30 | 89 ± 2 | 42 | 41 | 74 |
| DOMS-ZrN-40 | 89 ± 2 | 43 | 42 | 74 |
| DOMS-ZrN-80 | 90 ± 3 | 41 | 41 | 73 |

**TABLE IV.** Fit parameters of the PP curves obtained from the coatings and the SS316L substrate.

| Sample | $\beta_a$ (mV/decade) | $\beta_c$ (mV/decade) | $J_{corr}$ (nA/cm$^2$) | $E_{corr}$ (mV) | Corrosion rate ($\times 10^{-3}$ mm/year) |
|---|---|---|---|---|---|
| SS316L | $365 \pm 113$ | $121 \pm 2$ | $979 \pm 49$ | $-248 \pm 10$ | $10.2 \pm 0.5$ |
| dcMS-ZrN | $458 \pm 56$ | $281 \pm 46$ | $1398 \pm 23$ | $-245 \pm 4$ | $7.8 \pm 0.1$ |
| DOMS-ZrN-30 | $1056 \pm 510$ | $210 \pm 108$ | $525 \pm 111$ | $-225 \pm 8$ | $3.0 \pm 0.4$ |
| DOMS-ZrN-40 | $1890 \pm 88$ | $256 \pm 21$ | $615 \pm 14$ | $-214 \pm 1$ | $3.4 \pm 0.1$ |
| DOMS-ZrN-80 | $1074 \pm 68$ | $255 \pm 47$ | $486 \pm 5$ | $-212 \pm 3$ | $2.5 \pm 0.0$ |
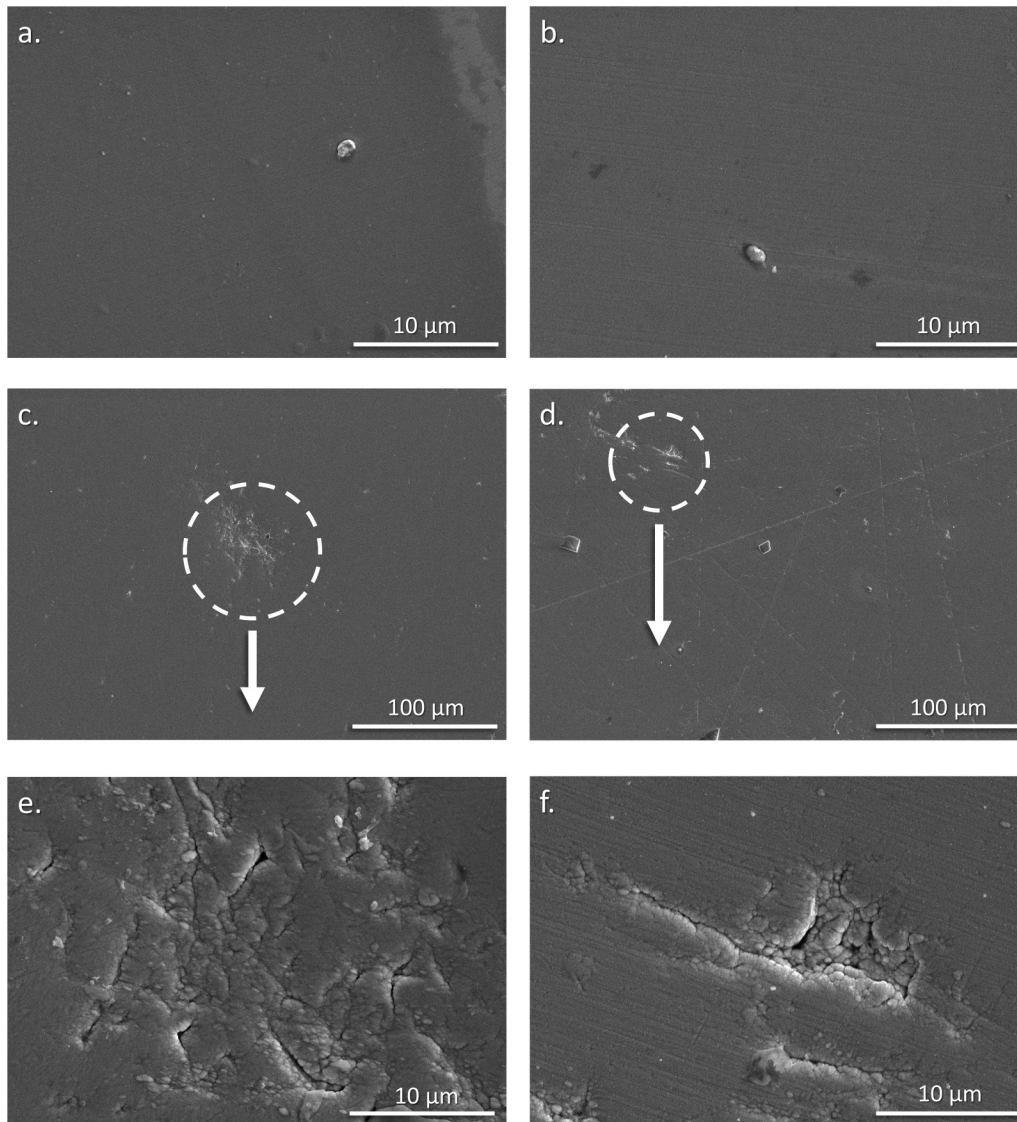


**FIG. 6.** SEM micrographs of the coatings DOMS-ZrN-80 [(a), (c), and (e)] and dcMS-ZrN [(b), (d), and (f)] after the PP tests. (a) and (b) correspond to the as-deposited condition.
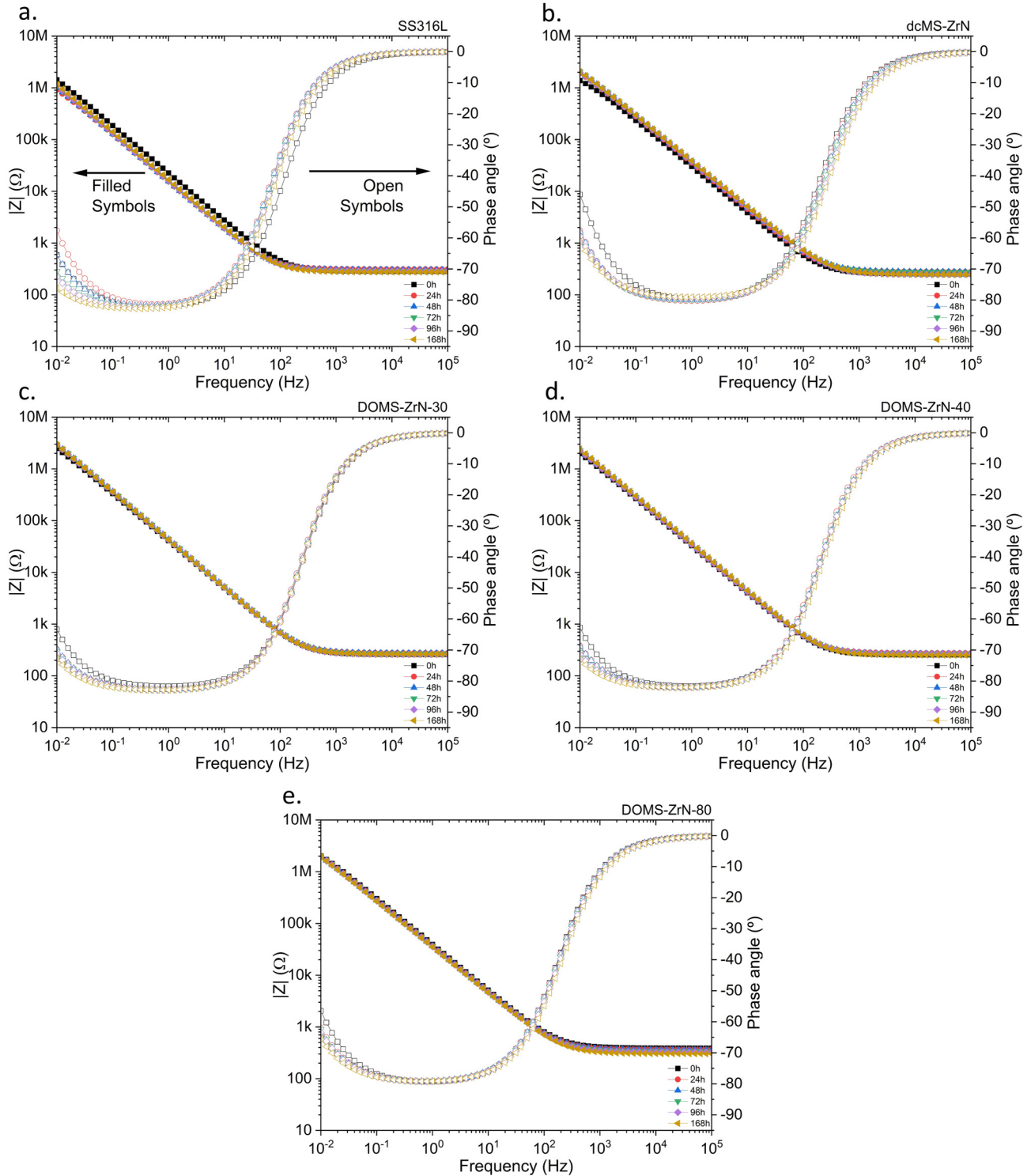
06 November 2024 11:23:08

**FIG. 7.** Bode and phase angle plots of the tested samples at different exposure times into simulated seawater: (a) SS316L, (b) dcMS-ZrN, (c) DOMS-ZrN-30, (d) DOMS-ZrN-40, and (e) DOMS-ZrN-80.

different among the films, which had different amounts of nitrogen according to the EDS quantification (see Table II). As the film was less metallic (higher amount of N), the corrosion current densities were lower and, consequently, the corrosion rates were lower too. The surface roughness did not seem to have an important influence on the corrosion behavior. This statement is easily verifiable if Fig. 4 and Table IV are assessed. Coincidentally, the sample (DOMS-ZrN-80) with the lowest Sa value showed the lowest corrosion rate. However, the sample with the highest roughness (DOMS-ZrN-40) did not show the highest corrosion rate. The influence of chemical composition and interactions between liquid/surface is crucial to explain the differences in corrosion behavior, which will be discussed later.

After the PP tests, the coated sample's surface did not exhibit catastrophic corrosion or failure events as large film detachments. Nevertheless, the surface shows some signs of chemical attack, as exhibited in Fig. 6. In general terms, the films exhibited NaCl crystals in several areas and some "cracks," as shown in Fig. 6. It is probable that these "cracks" originated from film defects, which acted as an initial point of local corrosion action, and according to Cubillos et al.,[49] these could be a posterior stage of pitting corrosion. However, these "cracks" zones are not representative of all the tested areas and probably this is the reason that the PP curves did not display any pitting characteristic event. As evidenced by Figs. 6(a). and 6(b), the films in the as-deposited condition did not show any apparent surface defect, but it is impossible completely to discard their presence.

Bode plots obtained after EIS tests at OCP from 0 until 168 h of exposure to artificial seawater are exhibited in Fig. 7. All the samples just showed the presence of a one-time constant at the intermediate frequency zone ($\sim10^{-1}$–10 Hz). Mejía et al.[50] described the appearance of two-time constants as common for porous coatings. Indeed, the films did not display this condition, which is coherent with the results shown by SEM (see Fig. 2) and AFM. According to Fig. 7, the coatings did not exhibit large variations in impedance modulus (|Z|) and phase angle along exposure time. Comparing |Z| values, all the samples obtained after 168 h of artificial seawater exposure exhibited higher impedance and, hence, better corrosion resistance than the uncoated substrate (SS316L), which always showed a value around 1 MΩ. Besides, the DOMS films grew differently as mentioned before (see Fig. 2) and the improvement of corrosion resistance was expectable since their growth profiles varied from fine columns at low nitrogen content to an unfeatured profile at higher nitrogen contents. This denser last profile causes difficulty in the penetration of any substance into the film. This increase in density is also the reason why the films obtained by DOMS exhibited higher |Z| values (better corrosion resistance) than their respective counterparts obtained by dcMS.

Regarding the phase angle, Fig. 7 shows the sample's variation along the exposure time at a lower frequency zone ($\sim10^{-1}$ to $10^{-2}$ Hz range). Commonly, the decrease in the phase angle at lower frequencies is connected to a corrosion rate increase,[51] and all the studied samples (films and uncoated substrate) showed this behavior after 168 h, which means an undoubted attack of artificial seawater over the studied surfaces. Additionally, plateau formation at intermediate frequencies in the bode plots of all films indicates a high capacitive response of the coating.[49]

Figure 8 shows the Nyquist plots at 0 and after 168 h of the samples. The rising of the imaginary part of impedance ($-Z_{img}$) after 168 h and, consequently, the shrinking of their real part of impedance ($Z_{real}$) in all studied samples are evident. Despite the reduction in $Z_{real}$, |Z| increased with time exposure as it is exhibited by the bode plots (see Fig. 7). The unique loop in all samples is notable, which is a clear indication of the absence of a diffusion
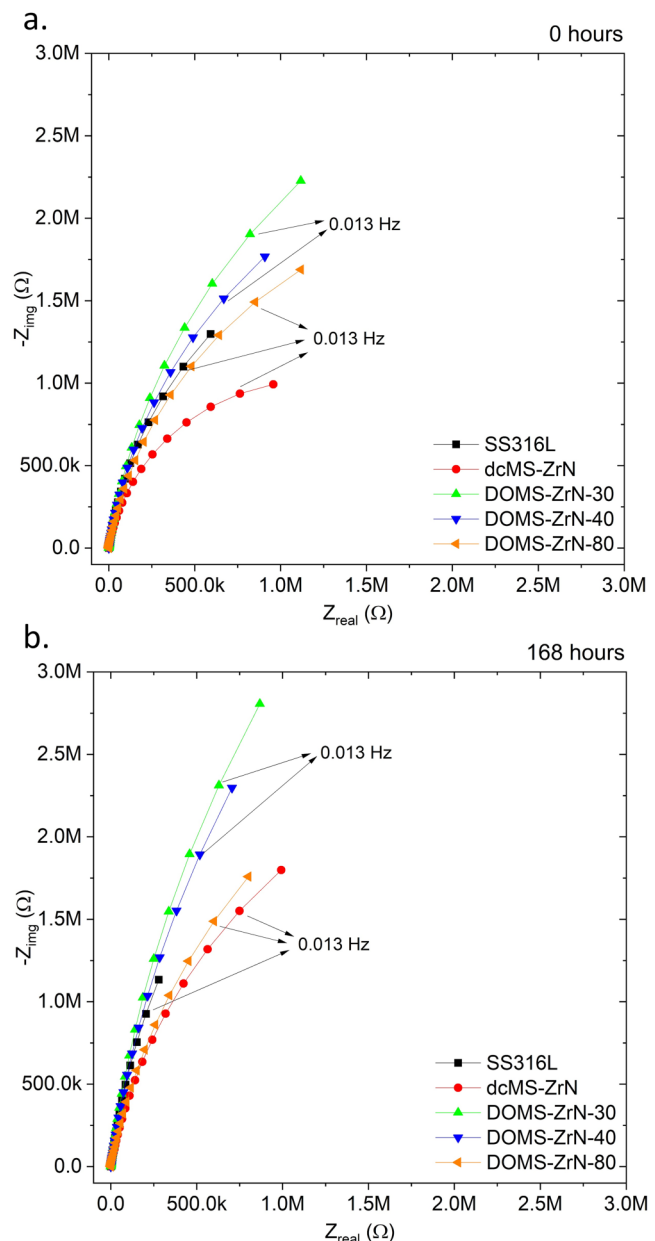


**FIG. 8.** Nyquist plots of SS316L and the films at 0 (a) and 168 h (b) exposure to simulated seawater.
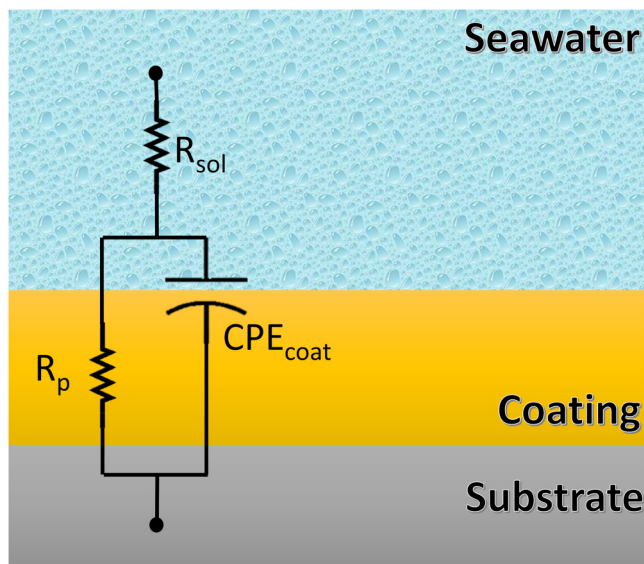
06 November 2024 11:23:08

**FIG. 9.** EEC schematic used to fit the electrochemical data measured in the films.

process or additional layers on the outermost part of the studied surfaces.

Figure 9 exhibits an equivalent electrical circuit (EEC) used to fit the EIS results, with their respective fit parameters displayed in Table V. The results show chi-square ($\chi^2$) values in the order of $10^{-3}$ and are considered a good fit according to several authors.[49,52] Concerning the EEC (Fig. 9), $R_{sol}$ represents the resistance of the electrolyte (artificial seawater), $R_p$ and $CPE_{coat}$ represent the polarization resistance of the film and the constant phase element of the coating. The CPE element is employed to fit the electrochemical reaction of the studied surface more precisely. In an ideal coating, the layer response would be a capacitor.[53] However, due to the presence of (chemical or physical) heterogeneities such as impurities or flaws, which are common in sputtered films in which CPE is employed. The exponent $\alpha$ of CPE can vary between 0 and 1, wherein 0 represents electrical resistance and 1 is pure capacitor behavior.[53] Table V shows $\alpha$ values around 0.9, confirming that the obtained films have capacitive behavior with some defects/impurities. Also, the dcMS film exhibited a lower $\alpha$ value than the DOMS film, which indicates that the HiPIMS processing decreased the

number of film defects. Concerning $R_p$, all the coatings showed a higher value than those obtained for the uncoated substrate and, hence, improved the corrosion resistance, confirming the PP test results (see corrosion rates of Table IV). Again, $R_p$ exhibited higher values in DOMS films than in dcMS films.

According to some authors,[15,54–56] the porosity index can be calculated quantitatively in films by Eq. (2),

$$ PI\ (\%) = \frac{R_P}{R_{P,c}} \times 10^{-\left|\frac{\Delta E_{corr}}{\beta_a}\right|}, \qquad (2) $$

where $R_p$ and $R_{p,c}$ correspond to the polarization resistance of the substrate and the coating, respectively. $\Delta E_{corr}$ is the difference between the substrate and coating corrosion potentials and $\beta_a$ is the anodic Tafel slope of the substrate.[56] The obtained values (see Table V) confirm, as discussed before, that the films are not porous and show a porosity index below 1.[57] The porosity index decreased in DOMS films up to 64% compared to dcMS films, which seems to impact the corrosion resistance positively.

## IV. SUMMARY AND CONCLUSIONS

Zirconium nitride films were obtained by R-HiPIMS. Regardless of the amount of nitrogen during the deposition, the films showed an evident dense growth profile typical of zone T of the Anders diagram. Besides, the chemical composition of the coatings showed a slight contribution of residual oxygen and a consistent increase of nitrogen amount as the $N_2$/Ar ratio increased during deposition. Changes in the film microstructure were evident. The fcc-ZrN and ort-$Zr_3N_4$ crystal phases were detected in all the films. The increase in the $N_2$/Ar ratio was directly related to a drop in the peak power of the Zr target and, consequently, to a shift of the preferential orientation of the ZrN crystal phase from (111) to (220). The detection of the $Zr_3N_4$ phase evidenced the inclusion of interstitial atoms in the ZrN lattice that created lattice deformations and, hence, the film structures were subjected to compressive residual stresses.

Concerning wettability, all the films showed similar surface free energy regardless of the nitrogen content or used input power source (dcMS or HiPIMS). The films showed low roughness ($S_a < 10\ nm$) and nitrogen addition during deposition, increasing the films' smoothness, i.e., reduction of $S_a$ values. Comparing the contact angles measured with artificial seawater, the DOMS films showed a phobic trend. The DOMS films achieved an ~8% work of adhesion reduction compared to the dcMS films and, hence, a higher seawater rejection.

**TABLE V.** EIS fit parameters of the coatings according to the EEC of Fig. 9.

| Sample | $R_u$ ($\Omega$) | $R_p$ (M$\Omega$) | $CPE_{coat}$ ($\mu S \ast s^\alpha$) | $\alpha$ | $\chi^2$ ($\times 10^{-3}$) | Porosity index (%) |
|---|---|---|---|---|---|---|
| SS316L | 289 ± 14 | 3.9 ± 1.5 | 11.1 ± 1.3 | 0.91 ± 0.00 | 1.3 | — |
| dcMS-ZrN | 268 ± 17 | 4.4 ± 1 | 5.8 ± 0.2 | 0.86 ± 0.00 | 5.1 | 0.851 |
| DOMS-ZrN-30 | 277 ± 12 | 9.9 ± 1.7 | 5.4 ± 0.1 | 0.90 ± 0.00 | 1.5 | 0.341 |
| DOMS-ZrN-40 | 279 ± 13 | 8.1 ± 1.6 | 5.8 ± 0.1 | 0.91 ± 0.00 | 2.0 | 0.388 |
| DOMS-ZrN-80 | 320 ± 17 | 10.1 ± 0.8 | 4.2 ± 0.2 | 0.90 ± 0.00 | 4.0 | 0.307 |

The EIS and PP tests were evidence of the best corrosion resistance as the nitrogen content increased in the DOMS films. The protection of films increased as corroborated by an ~3.3 times reduction in the corrosion rate compared to the uncoated substrate (SS316L) and an ~2.6 times reduction compared to the dcMS film. Besides, the porosity index proves a higher densification of the DOMS films and, thus, influences the corrosion resistance increase.

## ACKNOWLEDGMENTS

## AUTHOR DECLARATIONS

### Conflict of Interest

The authors have no conflicts to disclose.

### Author Contributions

**José D. Castro:** Data curation (lead); Formal analysis (lead); Investigation (lead); Visualization (lead); Writing – original draft (lead). **Beatriz Pinto:** Formal analysis (supporting); Investigation (supporting). **Fábio Ferreira:** Formal analysis (supporting); Validation (supporting); Writing – review & editing (equal). **R. Serra:** Formal analysis (supporting); Validation (supporting); Writing – review & editing (equal). **S. Carvalho:** Conceptualization (lead); Funding acquisition (lead); Methodology (lead); Project administration (lead); Supervision (lead); Writing – review & editing (lead).

## DATA AVAILABILITY

The data that support the findings of this study are available from the corresponding author upon reasonable request.

## REFERENCES

[1] J. D. Castro et al., Surf. Coat. Technol. **386**, 125464 (2020).

[2] B. Tuck, E. Watkin, A. Somers, and L. L. Machuca, npj Mater. Degrad. **6**, 25 (2022).

[3] A. Pistone, C. Scolaro, and A. Visco, Polymers **13**, 173 (2021).

[4] M. Graham and N. Cady, Coatings **4**, 37 (2014).

[5] G. D. Bixler and B. Bhushan, Adv. Funct. Mater. **23**, 4507 (2013).

[6] G. D. Bixler and B. Bhushan, Crit. Rev. Solid State Mater. Sci. **40**, 1 (2015).

[7] O. P. Abioye, C. A. Loto, and O. S. I. Fayomi, J. Bio-Tribo-Corros. **5**, 22 (2019).

[8] J. D. Castro, M. J. Lima, and S. Carvalho, Appl. Surf. Sci. **584**, 152582 (2022).

[9] E. Carneiro, J. D. Castro, S. M. Marques, A. Cavaleiro, and S. Carvalho, Surf. Coat. Technol. **418**, 127271 (2021).

[10] N. K. Manninen, S. V. Calderon, I. Carvalho, M. Henriques, A. Cavaleiro, and S. Carvalho, Appl. Surf. Sci. **377**, 283 (2016).

[11] D. Cavaleiro, D. Veeregowda, A. Cavaleiro, S. Carvalho, and F. Fernandes, Surf. Coat. Technol. **399**, 126176 (2020).

[12] R. W. Harrison and W. E. Lee, Adv. Appl. Ceram. **115**, 294 (2016).

[13] J. M. González-Carmona, J. D. Triviño, A. Gómez-Ovalle, C. Ortega, J. M. Alvarado-Orozco, H. Sánchez-Sthepa, and A. Avila, Ceram. Int. **46**, 24592 (2020).

[14] D. Cavaleiro, S. Carvalho, A. Cavaleiro, and F. Fernandes, Appl. Surf. Sci. **478**, 426 (2019).

[15] J. Jin, H. Liu, D. Zheng, and Z. Zhu, Int. J. Hydrogen Energy **43**, 10048 (2018).

[16] S. Calderon, C. F. A. Alves, N. K. Manninen, A. Cavaleiro, and S. Carvalho, Coatings **9**, 682 (2019).

[17] A. Baptista, F. Silva, J. Porteiro, J. Míguez, and G. Pinto, Coatings **8**, 402 (2018).

[18] B. C. N. M. de Castilho et al., Sci. Rep. **12**, 2342 (2022).

[19] O. O. Abegunde, M. Makha, K. Machkih, A. Ghailane, H. Larhlimi, Y. Samih, and J. Alami, J. Bio-Tribo-Corros. **8**, 73 (2022).

[20] C. F. A. Alves, R. Serra, R. Bayat, F. Ferreira, A. Cavaleiro, and S. Carvalho, Electrochim. Acta **423**, 140497 (2022).

[21] V. F. C. Sousa, F. J. G. Silva, H. Lopes, R. C. B. Casais, A. Baptista, G. Pinto, and R. Alexandre, Materials **14**, 5122 (2021).

[22] J. D. Castro, M. J. Lima, I. Carvalho, M. Henriques, and S. Carvalho, Appl. Surf. Sci. **555**, 149704 (2021).

[23] J. D. Castro, M. J. Lima, and S. Carvalho, Surf. Coat. Technol. **451**, 129050 (2022).

[24] S. Shiri, P. Ashtijoo, A. Odeshi, and Q. Yang, Surf. Coat. Technol. **308**, 98 (2016).

[25] G. G. Stoney, Proc. R. Soc. London Ser. A **82**, 172 (1909).

[26] S. P. Rodrigues, S. Carvalho, and A. Cavaleiro, Int. J. Adv. Manuf. Technol. **107**, 3931 (2020).

[27] S. K. Rawal, A. K. Chawla, R. Jayaganthan, and R. Chandra, Mater. Sci. Eng., B **181**, 16 (2014).

[28] M. Kalin and M. Polajnar, Appl. Surf. Sci. **293**, 97 (2014).

[29] H. J. Busscher, A. W. J. van Pelt, P. de Boer, H. P. de Jong, and J. Arends, Colloids Surf. **9**, 319 (1984).

[30] G102−89 (Reapproved 2015)´1, ASTM Int. **89**, 1 (2015).

[31] J. C. Oliveira, F. Fernandes, R. Serra, and A. Cavaleiro, Thin Solid Films **645**, 253 (2018).

[32] A. Anders, J. Appl. Phys. **121**, 171101 (2017).

[33] M. Ohring, Materials Science of Thin Films, 2nd ed. (Academic Press City, London, 2002).

[34] A. Anders, Thin Solid Films **518**, 4087 (2010).

[35] R. Lamni, E. Martinez, S. G. Springer, R. Sanjinés, P. E. Schmid, and F. Lévy, Thin Solid Films **447–448**, 316 (2004).

[36] P. Carvalho, A. C. Fernandes, L. Rebouta, F. Vaz, L. Cunha, U. Kreissig, N. P. Barradas, A. R. Ramos, and E. Alves, Nucl. Instrum. Methods Phys. Res., Sect. B **249**, 458 (2006).

[37] T. Kuznetsova, V. Lapitskaya, A. Khabarava, S. Chizhik, B. Warcholinski, and A. Gilewicz, Appl. Surf. Sci. **522**, 146508 (2020).

[38] Y. Purandare, A. Ehiasarian, A. Santana, and P. Hovsepian, J. Vac. Sci. Technol., A **32**, 031507 (2014).

[39] P. Carvalho et al., J. Appl. Phys. **98**, 023715 (2005).

[40] J. Pelleg, L. Z. Zevin, S. Lungo, and N. Croitoru, Thin Solid Films **197**, 117 (1991).

[41] W. J. Chou, G. P. Yu, and J. H. Huang, Thin Solid Films **405**, 162 (2002).

[42] F. Ferreira, J. C. Oliveira, and A. Cavaleiro, Surf. Coat. Technol. **291**, 365 (2016).

[43] R. N. Wenzel, Ind. Eng. Chem. **28**, 988 (1936).

[44] M. Jin, F. Thomsen, T. Skrivanek, and T. Willers, Advances in Contact Angle, Wettability and Adhesion (John Wiley & Sons, Hoboken, NJ, 2015), pp. 419–438.

[45] J. C. Fernandez-Toledano, T. D. Blake, P. Lambert, and J. De Coninck, Adv. Colloid Interface Sci. **245**, 102 (2017).

[46] D. K. Owens and R. C. Wendt, J. Appl. Polym. Sci. **13**, 1741 (1969).

[47] L.-H. Lee, Fundamentals of Adhesion (Springer US, Boston, MA, 1991).

06 November 2024 11:23:08

[48]M. Dinu, E. Mouele, A. Parau, A. Vladescu, L. Petrik, and M. Braic, Coatings **8**, 132 (2018).

[49]G. I. Cubillos, E. Romero, and A. Umaña-Perez, Sci. Rep. **11**, 1 (2021).

[50]C. P. Mejía, H. S. Vanegas, and J. J. Olaya, Coatings **12**, 754 (2022).

[51]H. Nady, M. M. El-Rabiei, and M. Samy, Egypt. J. Pet. **26**, 79 (2017).

[52]A. Kameneva and V. Kichigin, Appl. Surf. Sci. **489**, 165 (2019).

[53]A. Lasia, *Electrochemical Impedance Spectroscopy and Its Applications* (Springer, New York, NY, 2014).

[54]B. Elsener, A. Rota, and H. Böhni, Mater. Sci. Forum **44–45**, 29 (1991).

[55]A. OrjuelaG, R. Rincón, and J. J. Olaya, Surf. Coat. Technol. **259**, 667 (2014).

[56]H. Jiménez, J. J. Olaya, J. E. Alfonso, and C. A. Pineda-Vargas, Surf. Coat. Technol. **321**, 341 (2017).

[57]B. Matthes, E. Broszeit, J. Aromaa, H. Ronkainen, S. P. Hannula, A. Leyland, and A. Matthews, Surf. Coat. Technol. **49**, 489 (1991).

06 November 2024 11:23:08